

## Sub-annual to multi-decadal shoreline variability from publicly available satellite imagery

Kilian Vos\*, Mitchell D. Harley, Kristen D. Splinter, Joshua A. Simmons, Ian L. Turner

*Water Research Laboratory, School of Civil and Environmental Engineering, UNSW Sydney, 110 King Street, Manly Vale, NSW, 2093, Australia*



### ARTICLE INFO

**Keywords:**  
 Optical imaging satellites  
 Shoreline detection  
 Semivariogram analysis  
 Google earth engine  
 Landsat  
 Sentinel-2

### ABSTRACT

The ability to repeatedly observe and quantify the changing position of the shoreline is key to present-day coastal management and future coastal planning. This study evaluates the capability of satellite remote sensing to resolve at differing temporal scales the variability and trends in shoreline position along sandy coastlines. Shorelines are extracted from 30 + years of publicly available satellite imagery and compared to long-term in-situ measurements at 5 diverse test sites in Europe, Australia, the USA and New Zealand. These sites span a range of different beach characteristics including wave energy and tide range as well as timescales of observed shoreline variability, from strongly seasonal (e.g., Truc Vert, France), to storm-dominated (e.g., Narrabeen-Collaroy, Australia), to only minor annual to multi-annual signals (e.g., Duck, USA). For the 5 sites, the observed typical horizontal errors varied between a root-mean-squared error (RMSE) of 7.3 m and 12.7 m. An analysis of the typical magnitudes of shoreline variability at temporal scales ranging from a single month up to 10 years indicates that, by the implementation of targeted image pre-processing then the application of a robust sub-pixel shoreline extraction technique, the resulting satellite-derived shorelines are generally able to resolve (signal-to-noise ratio > 1) the observed shoreline variance at timescales of 6 months and longer. The only exception to this is along coastlines where minimal annual to multi-annual shoreline variability occurs (e.g. Duck, USA); at these sites decadal-scale variations are successfully captured. The results of this analysis demonstrate that satellite-derived shorelines spanning the past 30 years as well as into the future can be used to explore and quantify intra- and inter-annual shoreline behaviour at a wide range of beaches around the world. Moreover, it is demonstrated that present-day satellite observations are also capable of capturing event-scale shoreline changes (e.g. individual storms) that occur at timescales shorter than 6 months, where this rapid response exceeds the typical magnitude of shoreline variability. Finally, several practical coastal engineering applications are presented, demonstrating the use of freely-available satellite imagery to monitor inter-annual embayed beach rotation, rapid storm-induced shoreline retreat and a major sand nourishment.

### 1. Introduction

Sandy coastlines are dynamic regions that may undergo rapid advances and retreats driven by changing environmental conditions (Wright and Short, 1984), or exhibit longer-term erosion/accretion trends due to a range of factors, including an imbalance in sediment supply. Wind, waves and nearshore currents stir unconsolidated sediment and transport it seawards, landwards and alongshore, continuously reshaping the topography and bathymetry of sandy coastlines. Observing and quantifying these changes is essential for coastal managers, planners and researchers on many coastlines vulnerable to extreme oceanographic forcing (Barnard et al., 2017; Harley et al., 2017; Masselink et al., 2016). Whereas long-term coastline monitoring

programs are scarce and limited in geographical coverage (Barnard et al., 2015), growth in the availability of data from satellites provides the opportunity to analyse 30 + years of imagery with global coverage.

Among the different morphological features employed to understand how sandy coastlines move and evolve over time, the location of the shoreline is often regarded as a key variable by coastal practitioners (Douglas and Crowell, 2000). Observations of shoreline variability are essential to quantify long-term recession trends, regulate coastal development and design coastal protection (National Research Council, 1990). Shorelines are idealised as the dynamic interface between water and land (Dolan et al., 1980), and according to Boak and Turner (2005) there are two main categories of shoreline indicators: those that are based on a visibly discernible feature (e.g., instantaneous water line,

\* Corresponding author.

E-mail address: [k.vos@unsw.edu.au](mailto:k.vos@unsw.edu.au) (K. Vos).

vegetation line), or alternatively the intersection of the coastal profile with a specific elevation datum (e.g., the 0 m Above Mean Sea Level (AMSL)). Shoreline indicators of this first type can be obtained from aerial photography or oblique video imagery (Holman and Stanley, 2007), while the second group requires information on the beach topography, which at the present time is typically obtained via in-situ RTK-GNSS surveys (e.g., Aagaard et al., 2005; Harley et al., 2011) or 3D mapping technology such as Lidar or UAVs (e.g., Stockdon et al., 2002; Turner et al., 2016a). In-situ beach surveys provide highly accurate data (i.e., sub-metre accuracy) but are often limited in spatial extent and temporal resolution as they rely on human operators. Terrestrial video monitoring systems (Holland et al., 1997) are entirely unmanned and provide low-cost continuous data which encompasses a wide range of temporal scales (hours to years) and spatial scales (metres to a few kilometres). Yet, fixed cameras require a high vantage point and power supply and they cannot operate in areas where infrastructure is not available. In view of these constraints, only a limited number of sites in the world have been routinely monitored over the last three decades with either in-situ surveys or fixed cameras (e.g., Kuriyama, 2002; Lacey et al., 1998; Pianca et al., 2015; Różyński, 2005; Turner et al., 2016b; Van de Lageweg et al., 2013; Wijnberg and Terwindt, 1995) and long-term, uninterrupted time-series of shoreline variability and changes remain limited or absent along much of the world's coastlines.

Space-borne observations from satellites provide a potentially rich source of long-term historical shoreline datasets across spatial scales ranging from localised studies to unprecedented global applications. To highlight the vast amount of satellite data presently available, Fig. 1 presents a timeline of the major civilian Earth observation satellites carrying optical imaging sensors during the past four decades (refer also to Belward and Skøien (2015) and Elliott et al. (2016)). These missions include both publicly available satellites (i.e., operating under open-data policies) such as the Landsat series, ASTER and Sentinel-2, and commercial operations financed primarily on an ‘on demand’ basis targeted at tasked acquisitions for a customer-defined region of interest. With regards to publicly available satellites, a progressive increase in satellite optical image resolution is observed over the four decades, from 80 m pixel size for Landsat missions 1–3 (1972–1983), 30 m for Landsat 4–8 (1982 – present) and 10 m for Sentinel-2 (2015 – present). This increase in the available optical image resolution has been accompanied by a gradual increase in the satellite revisit period, from

every 18 days for Landsat 1–3, 16 days for Landsat 4–8 and 5 days for Sentinel-2.

Several recent studies have begun to report on the use of publicly available satellite imagery applied to the detection of shoreline change, with a primary focus on identifying long-term trends in shoreline position. For example, Almonacid-Caballer et al. (2016) characterised mid-term (5 years) changes in annual mean shoreline position using Landsat images of a low-energy beach, while Liu et al. (2017) employed 30 years of Landsat data to monitor changes in annual mean beach width and long-term shoreline behaviour of a wave-dominated beach. Xu (2018) quantified the yearly rate of shoreline change in the Gulf of Mexico using the Landsat archive and Hagenaaars et al. (2018) analysed the spatial variability in erosive/accretive yearly trends after a large-scale nourishment. Recently, Luijendijk et al. (2018) and Mentaschi et al. (2018) each report on attempts for the first time to undertake global-scale assessment of yearly shoreline change rates. Crucially, an investigation of the full range of temporal scales that can be resolved using satellite-derived shorelines is lacking. Extending beyond the present focus on changes in annual mean shoreline position and estimation of long-term trends, the full exploitation of the extensive public datasets depicted in Fig. 1 applied to shorter-term to seasonal timescales as well as annual variability and longer-term trends, is yet to be fully investigated and reported.

In this study, the capability to extract shoreline change data from publicly available satellite imagery at timescales from individual storm events, to months, seasons and several years and decades is assessed. To quantify the shoreline position a refined version of the sub-pixel resolution shoreline detection technique described in Liu et al. (2017) is applied, with the addition of an image classification component to refine the detection of the sand/water interface. To identify the full potential of satellite remote sensing to capture sub-annual to multi-decadal shoreline variability, the analyses presented is not limited to horizontal accuracy only, but also investigates the differing temporal scales of potential shoreline change (i.e., single storm events, beach rotation, cyclic-seasonal variability, long-term erosion/accretion trends, and engineering interventions) that can be resolved by shorelines extracted from satellite imagery.

In the following section 2, the five case sites used in this study are briefly described, and an overview provided of the optimised and robust sub-pixel resolution technique that is used to derive shoreline time-

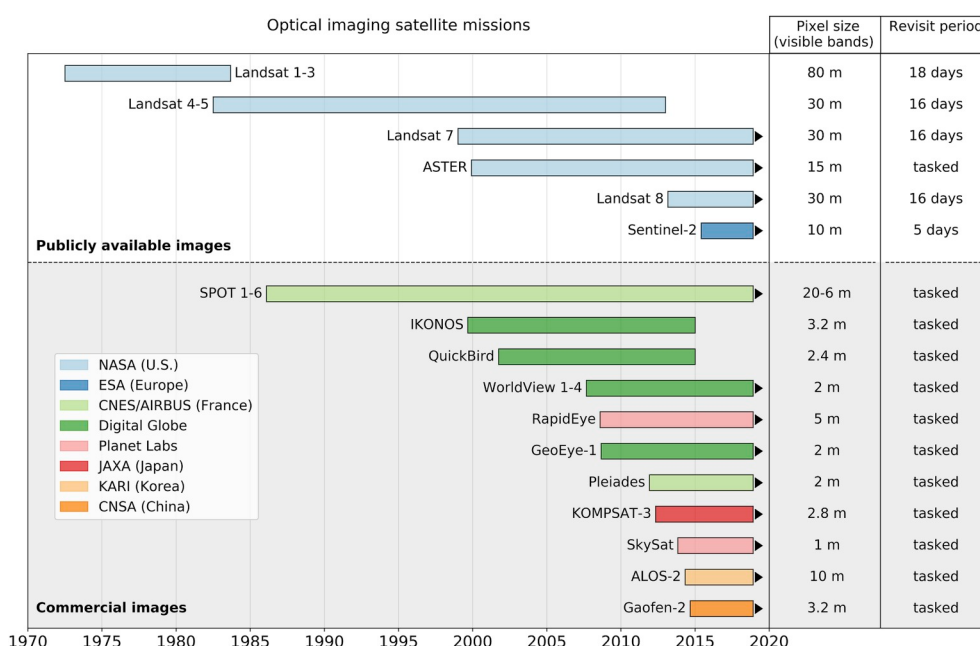


Fig. 1. Timeline for the major civilian Earth observation satellites operating optical imaging sensors with global coverage.

series from individual satellite images. In Section 3, long-term time-series of satellite-derived shoreline position are validated against in-situ shoreline datasets at the five study sites, followed by a semivariogram analysis of the typical magnitudes of shoreline variability over different timescales at each of these diverse sites. Several practical coastal engineering applications are presented in section 4, demonstrating the use of freely-available satellite imagery to monitor inter-annual embayed beach rotation, rapid storm-induced shoreline retreat and a major sand nourishment. The present limitations of satellite-derived shorelines are discussed in Section 5, followed by Conclusions in Section 6.

## 2. Methods

### 2.1. Study sites

To quantify and assess the capability of publicly available satellite imagery for inter-annual to multi-decadal shoreline change mapping, a total of five diverse study sites across three continents are considered here. These sites exhibit a range of different beach characteristics including variability in wave energy and tide range, as well as different temporal variability, from strongly seasonal, to storm-dominated, to only minor annual to multi-annual signals. The five sites were selected based on the availability of high-frequency (at least monthly) long-term ( $> 10$  years) in-situ shoreline data obtained from field surveys or on-site video monitoring. Table 1 summarises the key characteristics of each site (mean sand diameter  $D_{50}$ , characteristic beach face slope, mean spring tidal range and typical beach state as described by Wright and Short (1984)) and provides a short description of the available long-term shoreline data sets that are used for comparison and validation.

Narrabeen-Collaroy (hereafter simply referred to as 'Narrabeen') is a 3.6 km long embayment situated on the Northern Beaches of Sydney along the south-eastern coast of Australia. The tide regime is microtidal (mean spring range of 1.3 m) with a characteristic beach face slope of  $\sim 0.1$ . Narrabeen exhibits typically intermediate beach states and varies from Reflective to Longshore Bar Trough based on the Wright and Short (1984) classification. The 40 + year dataset (1976 – present) of monthly profile surveys along the five cross-shore transects indicated in Fig. 2 is described in detail in Turner et al. (2016b). The observed range of shoreline variability at Narrabeen over the 40 + year survey period varies from 80 m at transect NA1 to 55 m at transect NA4, and the observed dominant behaviour in shoreline response is forced by individual and/or sequential storm events (Harley et al., 2011).

Moruya is a 2.4 km long embayed beach located 300 km south of Narrabeen. The tide regime is also microtidal (mean spring tide range 1.3 m) with a similar characteristic beach face slope to Narrabeen (slope  $\sim 0.1$ ). Due to wave sheltering from offshore reefs, the beach state is typically between Reflective to Transverse Bar and Rip. Monthly topographic profile surveys using the Emery method (Emery, 1961) of three cross-shore transects at this site commenced in 2007. Large magnitude (up to 100 m) oscillations of the shoreline both in the cross-shore direction ('beach oscillation') and at alternative ends of the embayment ('beach rotation') are observed at inter-annual timescales (Short et al., 2014). The two end-member transects MO1 and MO3 are considered in this study.

Tairua beach is located along the east coast of the Coromandel Peninsula in the North Island of New Zealand. The tide regime is larger than the two Australian study sites and at the upper range for microtidal coastlines (spring tide range  $0 \sim 2$ m). The 1.2 km long embayed beach is characterised by a steep beach face slope ( $\sim 0.2$ ) and the typical beach state is intermediate (Blossier et al., 2016). A coastal imaging station situated at the southern end of the beach has been monitoring this site since 1999, resulting in a daily shoreline data set that now spans nearly two decades (Van de Lageweg et al., 2013). Since the horizontal accuracy of the video-monitoring system decreases with distance from the camera (ranging from 2 to 12 m along the beach

**Table 1**  
Beach characteristics of the study sites and description of the in-situ shoreline data sets.

Site	D50 (mm)	Characteristic beach face slope	Mean spring tidal range (m)	Mean deepwater sig. Wave height (m)	Typical beach state	Surveys undertaken	Survey start date	Survey method	Shoreline Proxy (m AMSL)	Reference publication
Narrabeen	0.3	0.1	1.3	1.6	Dissipative to Reflective	Monthly beach profiles	1976	Emery method and GNSS	0.7	Turner et al. (2016b)
Moruya	0.35	0.1	1.3	1.2	Intermediate to Reflective	Monthly beach profiles	2007	Emery method	0.7	Short et al. (2014)
Tairua	0.6	0.2	2	1.4	Intermediate	Daily shorelines	1999	Video monitoring	0.5	Van de Lageweg et al. (2013)
Duck	0.3	0.1	1.2	1.0	Intermediate	Monthly beach profiles	1981	CRAB	0.7	Larson and Kraus (1994)
Truc Vert	0.35	0.05	3.7	1.4	Intermediate	Monthly beach profiles	2005	GNSS	1.5	Castelle et al. (2014)

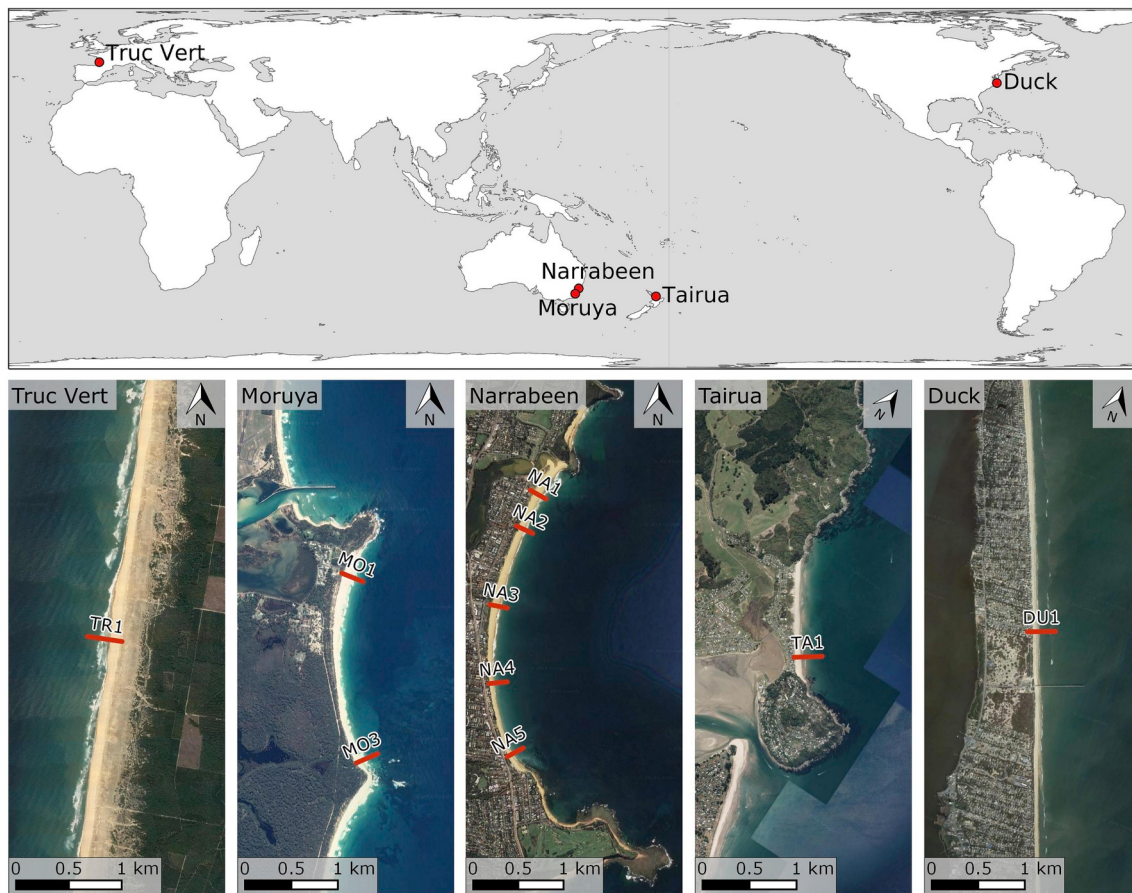


**Fig. 2.** World map showing the geographical location of the five study sites, from left to right: Truc Vert beach, France; Moruya beach, Australia; Narrabeen-Collaroy, Australia; Tairua, New Zealand; Duck, North Carolina, United States. At each site, the cross-shore transects employed to quantify shoreline displacement in this study are plotted in red. (For interpretation of the references to colour in this figure legend, the reader is referred to the Web version of this article.)

according to [Van de Lageweg et al., 2013](#)), a cross-shore transect located at the southern end of the beach (transect TA1) was chosen for this study to quantify shoreline changes at the site (see Fig. 2). The beach is subject to smaller magnitude cross-shore displacements of the shoreline ( $\sim 40$  m range) as well as rotation of the embayment planform ([Van de Lageweg et al., 2013](#)).

The beach at Duck in North Carolina, USA, is a world-renowned coastal monitoring centre, home to the U.S. Army Corps of Engineers Field Research Facility, where cross-shore transects have been surveyed monthly using a Coastal Research Amphibious Buggy (CRAB) and a military amphibious vehicle (LARC) since 1981 (e.g., [Larson and Kraus, 1994](#)). The site is an exposed, open beach located on the east coast of the United States, on a barrier island separating the Atlantic Ocean from mainland North Carolina. The tide regime is microtidal (mean spring tide range 1.2 m) with a characteristic beach face slope of 0.1. The typical beach state is intermediate. At this site, the relatively small shoreline variance signal is dominated by inter-annual variability ([Pianca et al., 2015](#)). A transect (DU1) located at the northern boundary of the Field Research Facility is considered in this study (see Fig. 2).

Truc Vert beach is situated in the south west of France along a 100 km-long stretch of exposed sandy coastline, where the much larger tide regime is classified as meso-macrotidal (mean spring tide range 3.7 m). The characteristic beach face slope is gentle ( $\sim 0.05$ ) and the beach typically exhibits a double-barred configuration: an intermediate (Transverse Bar and Rip) inner bar and a crescentic outer bar ([Sénéchal et al., 2009](#)). Monthly to bi-monthly topographic surveys using RTK-GPS have been collected since 2005, with a 1-year interruption in 2008. Progradation and retreat of the shoreline at this site are highly seasonal and no long-term trend has been observed ([Castelle et al., 2018](#)).

Moreover, because of the meso-macrotidal range and gentle slope, the beach intertidal region is wide (up to 100 m) and displays a complex morphology with intertidal bars, shoals and troughs ([Almar et al., 2012](#)). A cross-shore transect (TR1) was defined to quantify shoreline variability (see Fig. 2).

To obtain tide level data at each of the five study sites that is concurrent to the satellite-derived imagery used here, ocean water level data spanning the respective surveys periods were obtained from local tidal gauges (Duck, Truc Vert, Narrabeen and Moruya) and astronomical predictions (Tairua). The shoreline datum (or ‘proxy’) employed was the elevation of the 0.7 m AMSL contour at Narrabeen, Moruya and Duck (i.e., approx. Mean High Water Springs), the 1.5 m AMSL contour at Truc Vert (i.e., Mean High Water) and the 0.5 m AMSL contour at Tairua (i.e., elevation at which the shorelines were referenced by the video monitoring system). These shoreline datums have been found from previous studies to provide robust indicator of the shoreline variability at each local site.

## 2.2. Available satellite imagery and pre-processing

This section first summarises the sources, organisation and key characteristics (spatial resolution, spectral bands, etc) of current publicly available satellite imagery that, identifying those products are suitable for shoreline detection. Pre-processing of images, including the application of panchromatic image sharpening to increase image resolution where this is available, is then briefly described.

In the public archive of available satellite imagery (refer Fig. 1), Landsat images are organised as follows: the images that have a well-characterised radiometry (i.e., accurate spectral reflectance) and valid

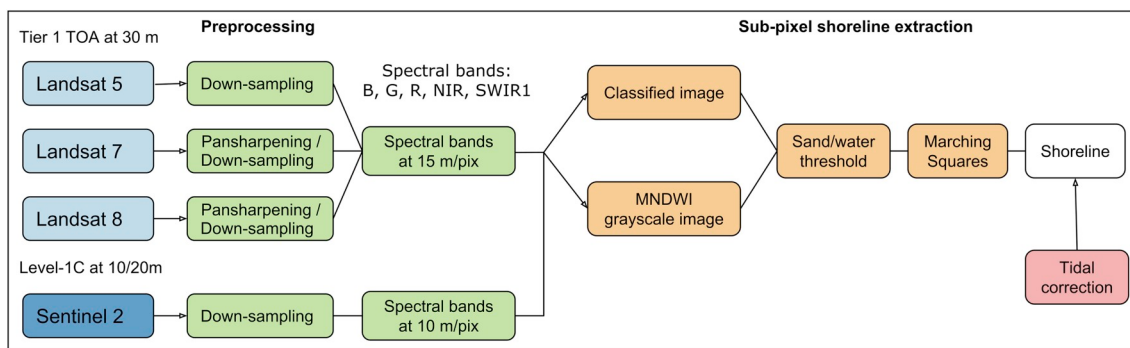


**Fig. 3.** Workflow diagram showing the step-by-step procedure to extract sub-pixel resolution shorelines from publicly available satellite imagery.

geometric accuracy ( $\text{RMSE} < 12\text{m}$ ) are placed in a folder known as Collection 1 Tier 1, while the rest of the images are placed in Collection 1 Tier 2. According to the data provider, only the Tier 1 scenes (i.e., images) are suitable for time-series analysis (USGS, 2017). For every Landsat Tier 1 image, three products are available: the *raw scene*, which only contains the digital-number (DN) values as measured by the sensor; the *Top-of-Atmosphere (TOA) reflectance image*, in which DN values have been converted to reflectance according to Chander et al. (2009); and the atmospherically corrected *Surface reflectance image*. The Top-of-Atmosphere (TOA) reflectance images were selected for this study as they provide a standardised comparison between images acquired on different dates or by different sensors (Chander et al., 2009). The Sentinel-2 equivalent of Landsat Collection 1 Tier 1 products are known as Level-1C products, which also contain quality-controlled TOA reflectance images that are suitable for time-series analysis (ESA, 2015). Accordingly, all the Tier 1 TOA satellite images from Landsat 4, Landsat 5, Landsat 7, Landsat 8 collections, as well as the Sentinel-2 Level-1C scenes, covering the study sites were retrieved with Google Earth Engine. Images from Landsat 1 to 3 were excluded from this study as they have a pixel size of 80 m and were therefore deemed to contain insufficient detail to map shorelines. Given the very limited number of Landsat 4 images available at the different sites ( $< 10$ ), Landsat 4 was also excluded. ASTER was not designed to continuously acquire data (tasked acquisitions only) and observations of episodic events such as volcanic eruptions, fires and floods are prioritised (Abrams and Hook, 2002). Since minimum coverage of the study sites is offered in the archive of ASTER scenes, this platform was also excluded from the present work.

Google Earth Engine (Gorelick et al., 2017) provides the capability to crop scenes to specific area of interest and select the relevant spectral bands before downloading individual imagery, significantly reducing the size of the files from several giga-bytes to approximately 1 megabyte per image for a 4 km-long beach. For shoreline detection applications, the relevant spectral bands are the visible bands (Blue, Green, Red), the near-infrared band (NIR) and the short-wave infrared band (SWIR1). The quality assessment (QA) band was also downloaded as it contains a cloud mask. Additionally, Landsat 7 and Landsat 8 images include a panchromatic band, a single-band image that combines the information from multiple spectral bands. The panchromatic band has a higher spatial resolution (i.e., 15 m) than the multispectral bands and is commonly employed to enhance the spatial resolution of the bands whose portion of the electromagnetic spectrum is covered by the panchromatic band. Following the approach of Liu et al. (2017), the panchromatic band was employed in the present study to increase the spatial resolution from 30 m to 15 m of the following spectral bands: 1) the Blue, Red, Green bands in Landsat 8 scenes; and 2) the Green, Red, NIR bands in Landsat 7 scenes. Panchromatic image sharpening was performed using a data fusion method based on principal component analysis (Tu et al., 2001). In this method, the multispectral bands are down-sampled to 15 m and decomposed in principal components, then

the first principal component is replaced by the panchromatic band (after histogram matching) and retransformed back into the original multispectral space. The bands that could not be pansharpened (NIR, SWIR1 in Landsat 8 scenes and Blue, SWIR1 in Landsat 7 scenes) were down-sampled to 15 m by bilinear interpolation. Landsat 5 scenes were also down-sampled as they do not include a panchromatic band. Sentinel-2 images have a higher spatial resolution: 10 m visible and near-infrared bands and a 20 m short-wave infrared band (SWIR1). To maintain the same resolution across all Sentinel-2 bands, the SWIR1 band was down-sampled to 10 m using bilinear interpolation. Finally, all the images with more than 10% cloud cover over the study site or georeferencing accuracy larger than 10 m were discarded.

### 2.3. Shoreline extraction from satellite imagery

A robust and generic algorithm to automatically extract the sandy shoreline at sub-pixel resolution from multispectral satellite imagery was then applied to the pre-processed imagery at all five study sites. This algorithm builds upon and extends the sub-pixel resolution border segmentation by Liu et al. (2017), originally proposed by Cipolletti et al. (2012). In this new method applied to the present study, an image classification component refines the segmentation into 4 distinct categories (described below) such that the thresholding method used to identify the shoreline is specific to the sand/water interface. As discussed below, this important modification results in a significantly more robust algorithm with the capability to consistently and correctly detect and map the sand/water interface at sites with quite different characteristics (e.g., urban/rural surroundings, presence/absence of an intertidal zone). The algorithm consists of three steps: 1) image classification into the four classes of ‘sand’, ‘water’, ‘white-water’ and ‘other land features’; 2) sub-pixel resolution border segmentation; and 3) tidal correction.

The overall methodology and workflow of image pre-processing then shoreline extraction are summarised in Fig. 3. Provided below is a brief summary of the three core shoreline extraction steps in this process: image classification, sub-pixel border segmentation and tidal-correction. For Readers who may wish to replicate and apply this optimised approach to obtain time-series of shorelines at their own site(s) of interest, an open-source Python toolkit, including facilitated access to the publicly available satellite imagery, is described in Vos et al. (2019) and available at <https://github.com/kvos/CoastSat>.

#### 2.3.1. Image classification

Since the instantaneous shoreline at sandy beaches is defined as the interface between land and ocean (Dolan et al., 1980), the first step is to find the pixels within every image that correspond to sand and water. However, along wave-dominated coastlines the boundary between sand and water is frequently characterised in imagery by the presence of white-water due to wave breaking, which is aerated water and therefore has a unique spectral signature. Consequently, a supervised

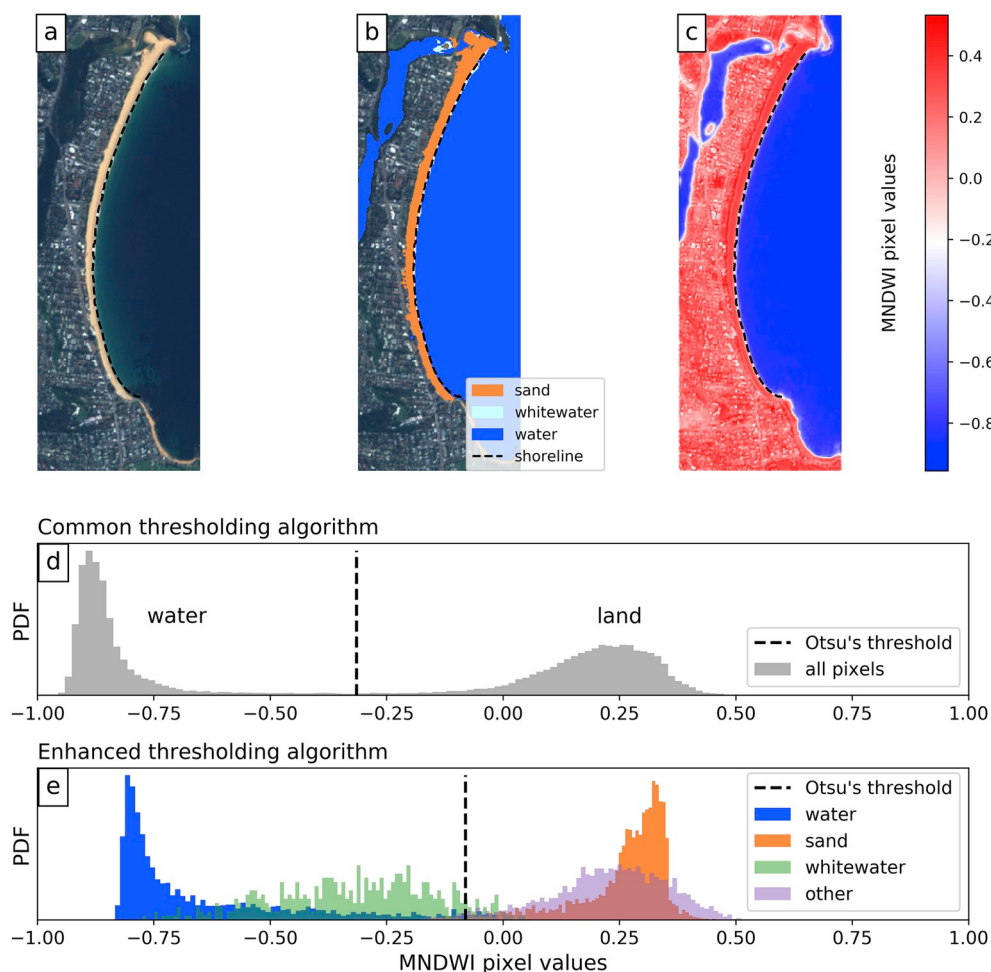


**Fig. 4.** a) RGB image of Narrabeen (from Sentinel-2). b) Output of image classification where each pixel has been labelled with one of three classes: sand, white-water and water (the 4th class “other land features” is not shown here for clarity). c) Grayscale (i.e., single colour band) image of the MNDWI pixel values. d) Histogram showing the probability density function of MNDWI values for all the pixels in the image. Commonly used thresholding algorithms find the threshold that maximises inter-class variance between the water and land modes (vertical dashed line). e) Histogram showing the probability density function of MNDWI values for each of the four classes (water, sand, whitewater and other land features). The classification refines the thresholding algorithm by obtaining the threshold that is specific to the sand/water interface, and ignoring the other land features and whitewater. (For interpretation of the references to colour in this figure legend, the reader is referred to the Web version of this article.)

classification scheme was employed to label each pixel of the image with one of four classes: ‘sand’, ‘water’, ‘white-water’ and a 4th class containing the other remaining land features (e.g., vegetation, buildings, rocks, coastal defence structures). A training set containing 1 500 pixels in each class (total 6 000) was manually digitised from satellite images at Narrabeen, to train a Neural Network (NN) classifier algorithm (called ‘Multilayer Perceptron’) that is commonly used for a wide range of applications including image classification and the generation of land cover maps (Kanellopoulos and Wilkinson, 1997). The NN classifier was trained with 70% of the data with the remaining 30% withheld to test and confirm 98% correct pixel classification. This approach was found to be satisfactory for the purposes image classification across all of the five study sites. For illustration, Fig. 4 includes an example Sentinel-2 satellite image (Fig. 4a) and the corresponding classified image (Fig. 4b).

### 2.3.2. Sub-pixel resolution border segmentation

The Modified Normalized Difference Water Index (MNDWI) is widely used to discriminate water from land features (Xu, 2006) and is calculated as follows:

$$\text{MNDWI} = \frac{\text{SWIR1} - \text{Green}}{\text{SWIR1} + \text{Green}} \quad (1)$$

where SWIR1 and Green are the pixel intensity in the short-wave infrared band (1.55–1.65 μm) and green band (0.52–0.6 μm). As shown in Fig. 4c, the MNDWI value is computed for each pixel, resulting in a grayscale (i.e., single colour band) image with values ranging from -1 to 1.

Previous shoreline studies have identified the boundary between

water and land by automatically thresholding the histogram of water index values for the entire image scene, which shows two distinct peaks as shown in Fig. 4d: negative values corresponding to water pixels and positive values to ‘land’ (Hagenaars et al., 2018; Kuleli et al., 2011; Liu et al., 2017; Luijendijk et al., 2018). In the present study, this blind use of a ‘land-water’ thresholding algorithm applied to the entire image is avoided, because images at the coast of course include individual pixels that may correspond to vegetation, rocky headlands, buildings and roads, as well as many other non-generic ‘land’ or ‘water’ features. Instead, a new and more targeted approach is adopted here, to specifically extract the boundary between water and sand pixels, ignoring the many other features that may be present and differ widely between individual study site locations. In Fig. 4e, the probability density function of MNDWI values is plotted for each of the four classes previously labelled (Section 2.3.1). This figure reveals that the water and sand classes are clustered around MNDWI values that are distant from each other, while the remaining two classes cover a broad range of MNDWI values and hence do not contribute in discriminating the sand/water interface. Accordingly, instead of calculating a global threshold as shown in Fig. 4d, we compute a more refined threshold that best divides the specific ‘sand’ and ‘water’ pixels only (Fig. 4e). This results in the detection of a much more stable and robust shoreline boundary through time. The histogram thresholding algorithm used here is an exhaustive search that maximises inter-class variance (Otsu, 1979). The final step of this algorithm is to map the iso-valued contour corresponding to the threshold value (MNDWI = -0.09 in this example) on the grayscale MNDWI map. This is implemented using a sub-pixel resolution contouring algorithm referred to as Marching Squares and described in Cipolletti et al. (2012).

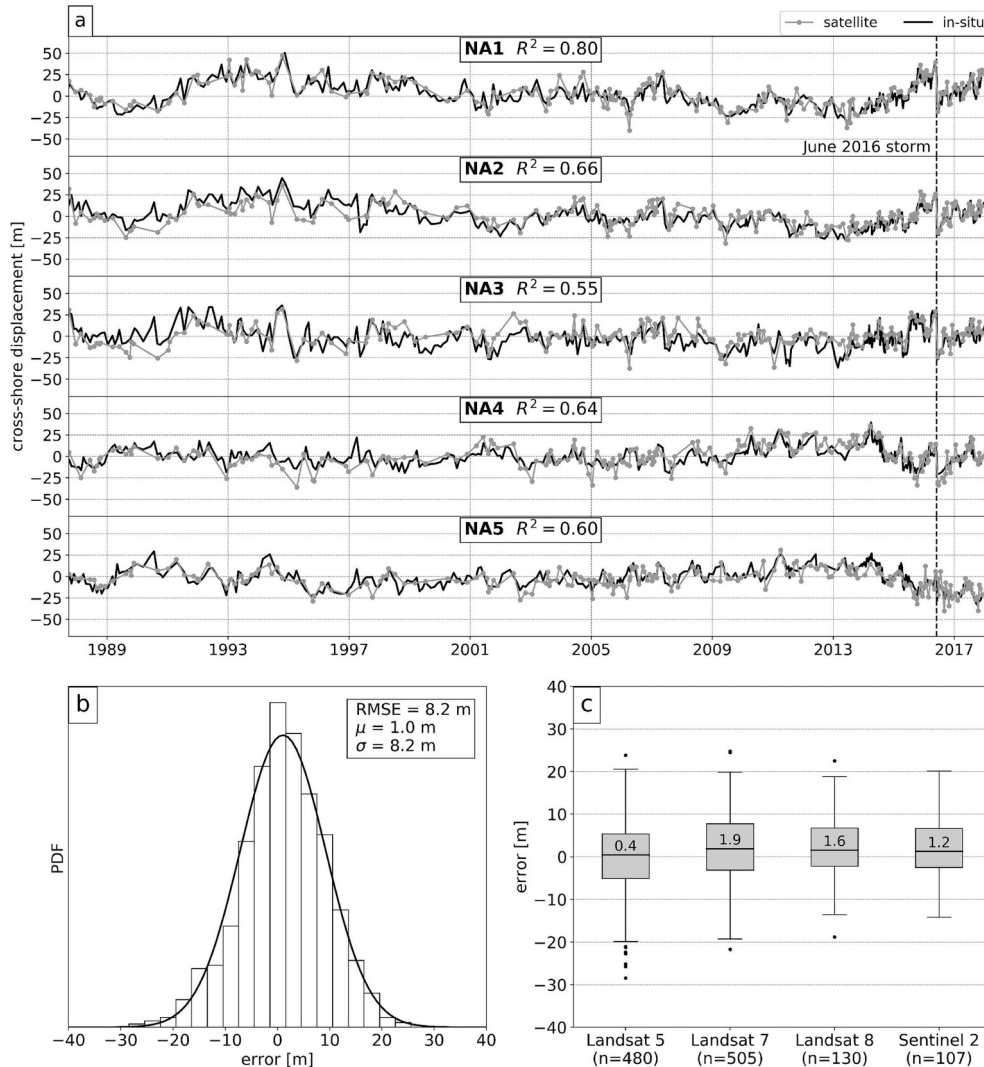


**Fig. 5.** a) Time-series of shoreline change along 5 transects at Narrabeen-Collaroy between 1987 and 2018 b) probability density function of the horizontal error (difference between in-situ measurements and satellite-derived chainages); c) boxplot of the horizontal errors for data points obtained from the different satellite missions.

At meso-macrotidal sites (i.e., Truc Vert), to limit the influence of complex intertidal features (shoals, bars, troughs) on the shoreline detection algorithm, only satellite images acquired at the higher stages of the tide ( $z_{\text{tide}} > 0.5$  m AMSL) are considered (see Section 5 for further discussion). For all other sites, images acquired across the full tidal cycle may be used for shoreline detection.

#### 2.3.3. Tidal correction

As satellite imagery is acquired at any stage of the tide, to enable inter-comparison, shorelines extracted from individual images must be projected to a single reference tidal datum at each site. To achieve this, a simple tidal correction is applied. This consists of translating horizontally the shoreline using a linear slope:

$$\Delta x = \frac{z_{\text{ref}} - z_{\text{tide}}}{m} \quad (2)$$

where  $\Delta x$  is the cross-shore horizontal shift,  $z_{\text{ref}}$  is the reference tidal datum,  $z_{\text{tide}}$  is the measured (or modelled) water level at the time of image acquisition, and  $m$  is a characteristic beach face slope specific to the site of interest. The final cross-shore position of satellite-derived shorelines are computed by intersecting shorelines with the cross-shore transects of interest (for example, those indicated in Fig. 2) and applying the corresponding tidal correction  $\Delta x$ .

The representative slope values reported in Table 1 were used to perform the tidal corrections in this study. To illustrate the advantage of including this third and final step of correcting each image for the tide, an improvement in mean error ranging from 5 m (Narrabeen) to 15 m (Truc Vert) was observed across the five diverse study sites considered here. The implications of a constant slope assumption are further discussed in Section 5.

#### 2.4. Temporal scales of shoreline variability - semivariogram analysis

Previous studies have focused on the horizontal accuracy that is achievable using satellite-derived shorelines, however the analysis of horizontal accuracy alone is not sufficient to inform the temporal scales of shoreline variability that can be resolved. Therefore, to identify the strengths and limitations of the satellite-derived method in capturing typical sub-annual and inter-annual shoreline variations at any site of interest, a more advanced analysis is presented in this section.

To quantify the typical magnitudes of shoreline variability from sub-annual to decadal timescales, Harley et al. (2011) proposed the use of semivariogram analysis. The empirical semivariogram estimates typical magnitude of change between pairs of points at a temporal lag  $h$  (i.e., timescale). The empirical semivariance (in units of  $\text{m}^2$ ) is computed from the time-series of shoreline cross-shore displacement  $d(t)$ :

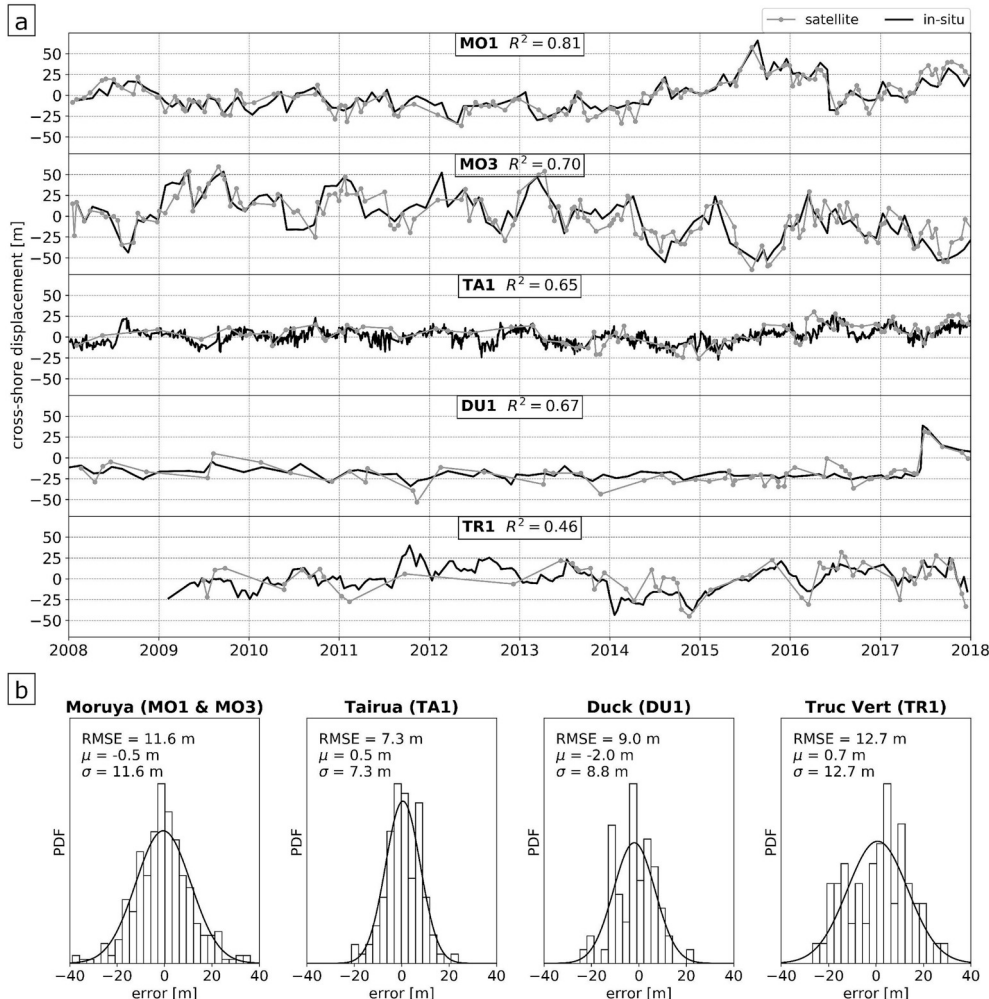


**Fig. 6.** a) Time-series of shoreline change at the four other sites since 2008. The complete time-series comparison for the sites that have in-situ that prior to 2008 are included in the Supplementary material. b) probability density function of the horizontal error (difference between in-situ measurements and satellite-derived displacements) for each site.

$$\gamma(h) = \frac{1}{2N(h)} \sum_{i=1}^{N(h)} [d(t+h) - d(t)]_i^2 \quad (3)$$

where  $N(h)$  denotes the number of data pairs at lag  $h$ . This method was employed at each of the five study sites to estimate typical magnitudes of shoreline variability within the in-situ shoreline measurements (field surveys or video) at lags (or timescales) of 1 month, 6 months, 1 year and 1 decade.

To quantify the degree to which the satellite-derived shorelines at each of the five sites could resolve the observed temporal scales of variability, an analysis of the measurement accuracy relative to the shoreline variability was performed. In many fields, the signal-to-noise ratio (SNR) is adopted as a measure of how much useful information there is in a system. Here, following Harley et al. (2011), the SNR is defined as the ratio between the typical magnitude of shoreline variability (at a certain timescale) and the observed measurement error. This SNR is therefore calculated as the ratio between the square-root of the semivariance ( $\sqrt{\gamma(h)}$ ) defined in Equation (3) of observed shoreline behaviour for a given lag (i.e., 1 month, 6 months, 1 year, 1 decade) and the horizontal accuracy (as a standard deviation) of the satellite measurements:

$$SNR = \frac{\sqrt{\gamma(lag)}}{\sigma_{satellite}} = \frac{\sigma_{lag}}{\sigma_{satellite}} \quad (4)$$

Values of  $SNR > 1$  indicate that the shoreline signal is increasingly dominant over the measurement error and hence the satellite-derived measurements are able to distinguish a change in shoreline position.  $SNR$  values  $< 1$  meanwhile denote signals that are indistinguishable from measurement noise and thus no physical change can be detected using satellite-derived shorelines at that particular timescale.

### 3. Results

#### 3.1. Time-series of shoreline change

The combined Landsat 5–8 and Sentinel-2 image datasets were used to extract time-series of shoreline change at each of the five sites using the shoreline detection methods described above. To illustrate, at Narrabeen-Collaroy a total of 502 satellite-derived shorelines were extracted between 1987 and 2018. Fig. 5a compares the two time-series of cross-shore shoreline displacement along the five transects at this site (shown in Fig. 2) derived from satellite images and from in-situ (field survey) measurements. The coefficient of determination ( $R^2$ ) varies between 0.80 at transect NA1 and 0.55 at transect NA3. The overall distribution of the horizontal error is presented in Fig. 5b, the RMSE is 8.2 m with 90% of the errors falling within 14 m. In Fig. 5c the horizontal errors are grouped by satellite mission (i.e., Landsat 5–8 and Sentinel-2). This analysis reveals that no significant difference is observed between the error distribution of data points

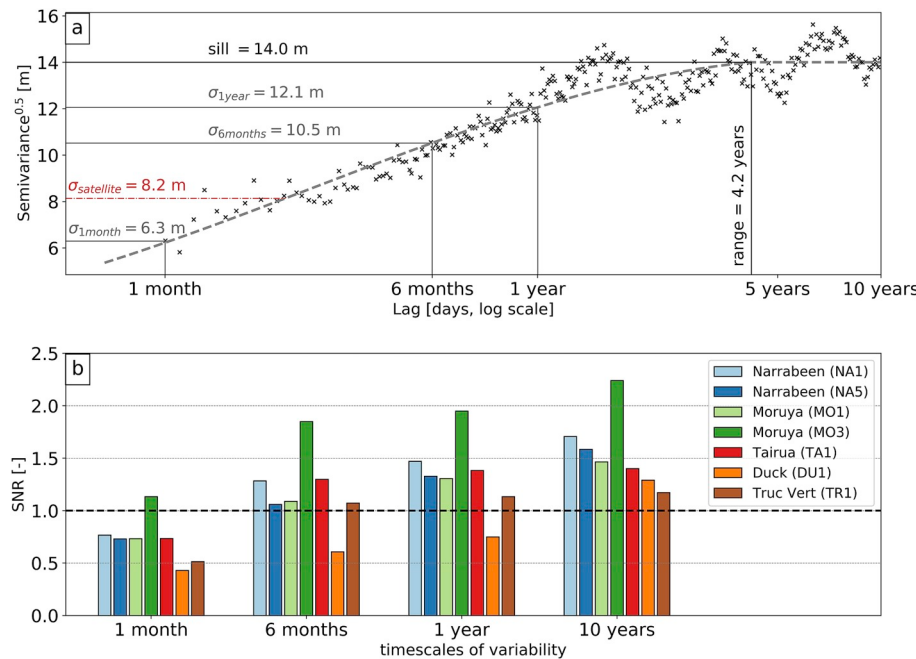


**Fig. 7.** a) Empirical semivariogram (converted to units of meters) for NA1 at Narrabeen-Collaroy. It shows typical cross-shore shoreline variability at different timescales, from monthly lags to 10 years lags. The dashed grey line is a smooth fit across the data points. The range and sill are also indicated on the figure. b) Signal-to-noise ratio analysis across different timescales. Values of SNR above the threshold of 1 denote shoreline signals that are increasingly dominant over the measurement error.

obtained from Landsat 5, Landsat 7, Landsat 8 and Sentinel-2. This is in spite of pixel resolutions varying in the different satellite missions from 30 m for the older Landsat 5 images to 10 m for the most recent Sentinel-2 data.

Similarly, the time-series of both satellite-derived and in situ (field survey or video) shoreline measurements were compared at the other study sites (Fig. 6). To facilitate direct visual comparison, only the period of time during which in-situ measurements were available at all sites (2008 onwards) is shown here; but the complete time-series for all sites can be found in the Supplementary Material (Figs. S1 to S3). At Moruya, the large magnitude oscillations that took place during the past decade are well captured by the satellite observations ( $R^2 = 0.81$  and 0.70 at transects MO1 and MO3, respectively). At Tairua the magnitude of the shoreline variations is much smaller, however the satellite-derived shorelines are able to identify correctly the major cross-shore displacements ( $R^2 = 0.65$ ). The shoreline at Duck also undergoes small-magnitude cross-shore fluctuations, with the exception of a large accretion in mid-2017, which is fully resolved by the satellite-derived measurements. Using only the higher stage of the tide imagery from Truc Vert (and therefore necessarily a lower sampling frequency), the time-series of satellite-derived shoreline variability and trends exhibit reasonable agreement with the in-situ surveys ( $R^2 = 0.46$ ); for example, significant erosion events that occurred during the northern hemisphere winters of 2015 and again in 2016 are well captured and quantified. The horizontal error statistics for each site are presented in Fig. 6b. The root-mean-squared error (RMSE) ranges between 7.3 m at Tairua and 12.7 m at Truc Vert.

### 3.2. Temporal scales of shoreline variability

The empirical semivariogram at the example Narrabeen field survey transect NA1, converted to units of metres ( $\sqrt{y(h)}$ ), is plotted in Fig. 7a and depicts the typical variability spanning 42 years of observations for monthly to decadal timescales at this location. The magnitude of typical shoreline change is shown to increase as lags (timescales) become longer, until becoming asymptotic to a ‘sill’, which indicates the overall variability of the shoreline for this example is 14 m, at a range of 4.3 years.

Generically, the smallest timescale at which typical variability can be estimated by semivariogram analysis is dictated by the frequency at which the in-situ measurements are available (e.g., daily, monthly, bi-monthly, etc). At transect NA1 (Fig. 7a) where the shoreline has been measured in the field every month since 1976, the typical magnitude of variability at lags of 1 month, 6 months, 1 year and 1 decade is respectively 6.3 m, 10.5 m, 12.1 m and 14 m, while the horizontal accuracy of the satellite measurements ( $\sigma_{\text{satellite}}$ ) is 8.2 m, as indicated in Fig. 5b. In the same way, typical magnitude of shoreline variability was characterised at the other sites. Table 2 summarises these results, comparing typical shoreline variability from monthly to decadal timescales at each of the available study transects. For clarity, at Narrabeen only transects NA1 and N5 are reported as they reflect the embayment wide shoreline variability. Across all these sites, the largest shoreline variance is observed at Moruya (see Fig. 6a), with transect MO3 having a typical variability of more than 20 m at lags longer than 6 months. In contrast, at Duck the shoreline exhibits the smallest typical magnitude of change, only reaching values above 10 m at decadal timescales. At Truc Vert, 90% of the overall variability is observed at a lag of 6 months, reflecting the strong seasonality observed at this site. The smallest decadal variability occurs at Tairua, with a sill ( $\sigma_{1 \text{ decade}}$ ) of 10.5 m.

**Table 2**

Magnitudes of shoreline variability at timescales of 1 month, 6 months, 1 year and 1 decade. Bold values indicate where the variance in the signal exceeds that of the satellite accuracy (standard-deviation calculated from the entire time-series included in the Supplementary Material).

Cross-shore Profiles	$\sigma_{1 \text{ month}}$ (m) <	$\sigma_{6 \text{ months}}$ (m)	$\sigma_{1 \text{ year}}$ (m)	$\sigma_{1 \text{ decade}}$ (sill) (m)	$\sigma_{\text{satellite}}$ (m)
Narrabeen NA1	6.3	10.5	12.1	14	8.2
Narrabeen NA5	6	8.7	10.9	13	8.2
Moruya MO1	8.5	12.6	15.2	17	11.6
Moruya MO3	<b>13.1</b>	21.5	22.6	<b>26</b>	11.6
Tairua TA1	5.5	9.7	10.4	10.5	7.4
Duck DU1	4	5.6	7	<b>12</b>	9.3
Truc Vert TR1	6.6	<b>13.7</b>	14.5	15	12.8

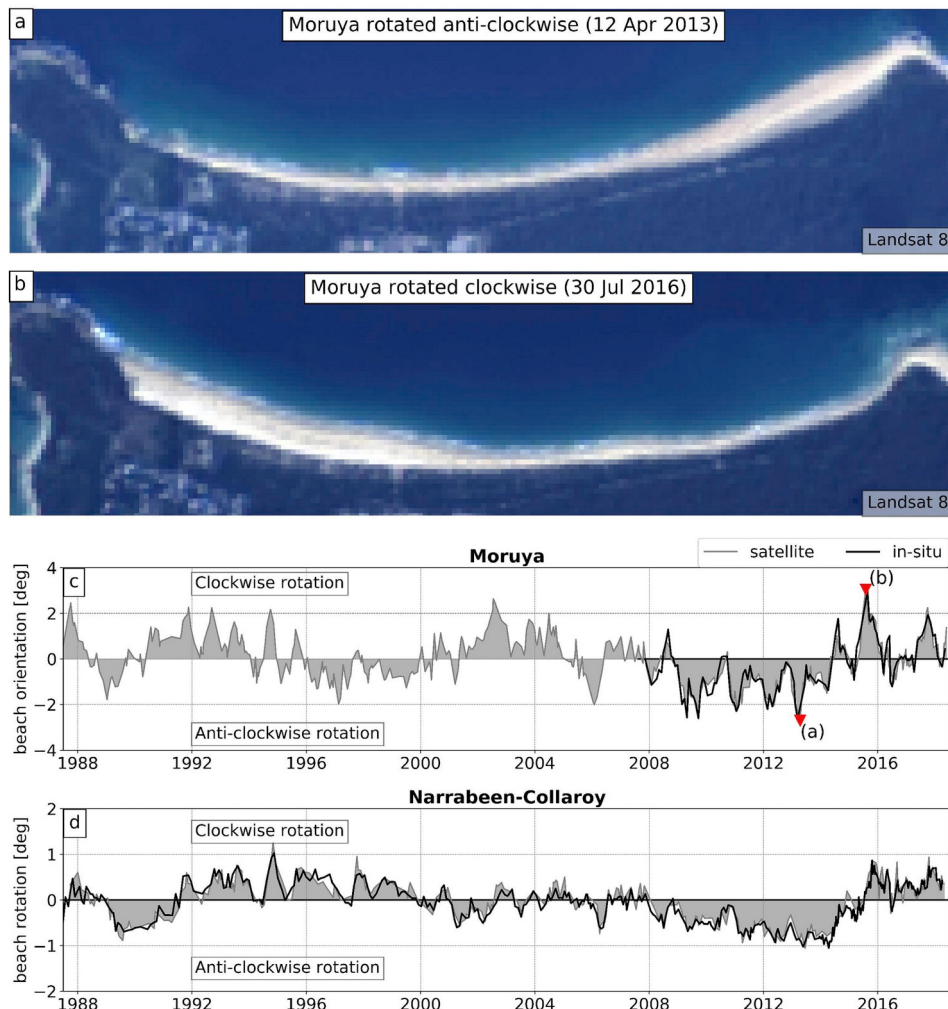


**Fig. 8.** a) Satellite image of Moruya rotated anti-clockwise. b) Satellite image of Moruya rotated clockwise. c) Time-series of the beach rotation index (in degrees) at Moruya derived from in-situ surveys and satellite-derived shorelines. Positive values indicate a clockwise rotation with respect to the long-term average, while negative values indicate anti-clockwise rotation. The red triangles indicate the dates in which the satellite images above were acquired. d) Time-series of the beach rotation index at Narrabeen-Collaroy. (For interpretation of the references to colour in this figure legend, the reader is referred to the Web version of this article.)

To identify the timescales at which the shoreline signal can be resolved by the satellite-derived observations, the SNR was computed at each site across a range of temporal scales and the results presented in Fig. 7b. With the exception of Duck, where the sub-annual to inter-annual shoreline signal is quite small, satellite derived shorelines have a  $\text{SNR} > 1$  for timescales longer than 6 months. At a decadal scale, SNR is higher than 1 for all sites, while at monthly timescales the SNR falls below 1 for all transects except MO3. Crucially, this reveals that satellite-derived shorelines can be used to examine intra- and inter-annual shoreline behaviour at a wide range of beaches around the world where a measurable shoreline variance is present.

#### 4. Example applications of satellite-derived shoreline measurements at different timescales

##### 4.1. Inter-annual variability: beach rotation

The above analysis of the accuracy of satellite-derived shorelines relative to typical magnitudes of shoreline variability and timescales suggests that shoreline measurements derived from publicly available satellite imagery can be used for a wide range of applications, extending well beyond the identification of long-term trends. Choosing an indicative threshold of 1 for the SNR, whereby the physical change in shoreline position exceeds the measurement error, the semivariogram

analysis (Fig. 7b) indicates that satellite observations can be reasonably anticipated to resolve typical variability of more than 6 months at four of the five diverse sites included in this study. The exception within our study, is Duck, NC, where the underlying inter-annual to annual shoreline variance is relatively minor, in which case only decadal variations may be realistically captured.

Embayed beach rotation is an example of shoreline change that occurs at seasonal to inter-annual timescales (e.g., [Masselink and Pattiaratchi, 2001](#); [Van de Lageweg et al., 2013](#)). Both Narrabeen and Moruya are previously reported to exhibit a beach rotation signal, alternating clockwise and anti-clockwise phases at inter-annual timescales ([Harley et al., 2015](#); [Short et al., 2014](#)). The Beach Orientation Index provides a practical measure of whether the orientation of the beach planform is more clockwise or anti-clockwise with respect to the long-term average. As in other studies ([Harley et al., 2014](#); [Ojeda and Guillén, 2008](#)), this index is calculated as the angle of the linear fit between the cross-shore displacements along the transects and their associated alongshore locations. To illustrate, Fig. 8 shows two Landsat 8 satellite images of Moruya acquired during anti-clockwise (Fig. 8a – April 2013) and clockwise (Fig. 8b – July 2016) phases of beach rotation. Fig. 8c and d compare time-series of the Beach Orientation Index (in degrees) at Moruya and Narrabeen derived from both in-situ measurements and satellite observations. It is evident that the satellite-derived beach orientation time-series reveal exactly the same patterns and

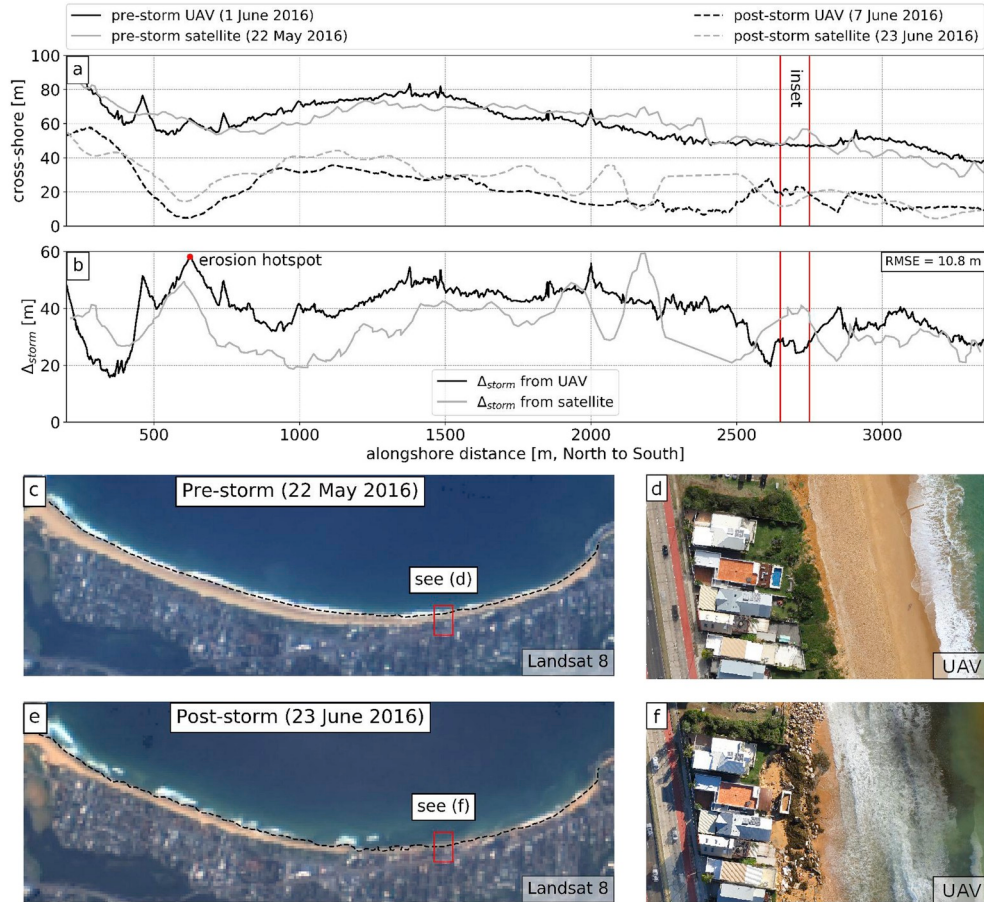


**Fig. 9.** a) Comparison between pre- and post-storm shorelines at Narrabeen obtained from UAV surveys and satellite images. The x and y axis respectively correspond to alongshore and cross-shore coordinates. Note that there are approx. 10 days between the UAV surveys and the closest satellite images. b) Alongshore variability of the pre/post-storm cross-shore displacement ( $\Delta_{\text{storm}}$ ). c) Pre-storm satellite image (15 m/pixel) acquired on the 22 May 2016. d) Post-storm satellite image acquired (15 m/pixel) on the 23 June 2016. e) Pre-storm UAV orthomosaic (3 cm/pixel). f) Post-storm UAV orthomosaic (3 cm/pixel).

magnitude of fluctuations between clockwise and anti-clockwise embayment rotation phases at both sites. Notably, while at Moruya in-situ measurements only started in 2007, the additional 20 years of data provided by the satellite imagery now enables the extension of this embayment rotation analysis back to the 1980's. Intriguingly, while both embayments exhibit similar behaviour during the past 10 years, they are observed to be out of phase when a longer period is considered, highlighting the importance of long-term sustained monitoring along coastlines. While previous studies have related inter-annual beach rotation at Narrabeen to variability in wave climate forced by El-Niño Southern Oscillation (Ranasinghe et al., 2004; Short and Trembanis, 2004), these new satellite-derived results from Moruya - located just 300 km south of Narrabeen - now suggest this proposed ENSO link may not be valid at a regional scale. Satellite remote sensing offers the possibility to investigate further the regional-scale coastline response to inter-annual modes of climate variability at other coastlines around the world.

#### 4.2. Capturing rapid shoreline change events

While the semivariogram analyses presented in Section 3.2 can be used to indicate the typical (i.e., average) magnitudes of shoreline variability at any site of interest, rapid episodic shoreline changes that occur due to extreme events such as a large coastal storm can considerably exceed these typical values. For instance, beach erosion caused by coastal storms may result in a significant landwards shift of the shoreline, while sand nourishments may lead to accelerated progradation of the shoreline.

To illustrate, in June 2016 an extratropical cyclone caused severe erosion along the southeast coastline of Australia (Harley et al., 2017). As highlighted in Fig. 5a, this resulted in the observation at Narrabeen

of shoreline retreated in the range of 40–60 m along the more northern transects NA1, NA2 and NA3. While the results in this figure show that the satellite-derived observations captured well (< 5 m error on the total shoreline recession) the cross-shore shoreline displacement caused by this storm at the locations of the five historical survey transects, by examining the continuous satellite-derived shorelines that extend along the full 3.6 km long embayment, additional insight into the alongshore variability of this rapid beach response is also obtained. In Fig. 9, pre- and post-storm shorelines measured by Unmanned Aerial Vehicle (UAV) 3D-surveys (Turner et al., 2016a) are compared to the shorelines extracted from the closest (in time) pre- and post-storm satellite images. Fig. 9b compares the UAV- and satellite-derived shoreline retreat ( $\Delta_{\text{storm}}$ ) showing that the satellite data is able to capture the magnitude of erosion caused by the storm event (mean error = 5.5 m and RMSE = 10.8 m). Significantly, the satellite-derived data is also able to identify more localised erosion 'hotspots' within the embayment, for instance, close to the north end of the beach (~200 m–~350 m alongshore) indicated in Fig. 9b. However, due to insufficient image resolution, the satellite imagery used to map the pre- and post-storm shorelines (Fig. 9c and e) cannot resolve the post-storm damage to beach-front property and infrastructure; this application requiring finer spatial scales such as the corresponding 3 cm/pixel UAV imagery depicted in Fig. 9d and f.

Another example of episodic shoreline change where the magnitude of response may exceed the 'typical' shoreline variability at the site, is illustrated by the extensive sand nourishment that occurred at Duck during the northern hemisphere spring of 2017. Fig. 10 shows two satellite images acquired at the commencement (May 2017) and upon completion (June 2017) of the sand nourishment project, as well as time-series of the shoreline cross-shore displacement along the DU1 transect between April and December 2017. This nourishment, which

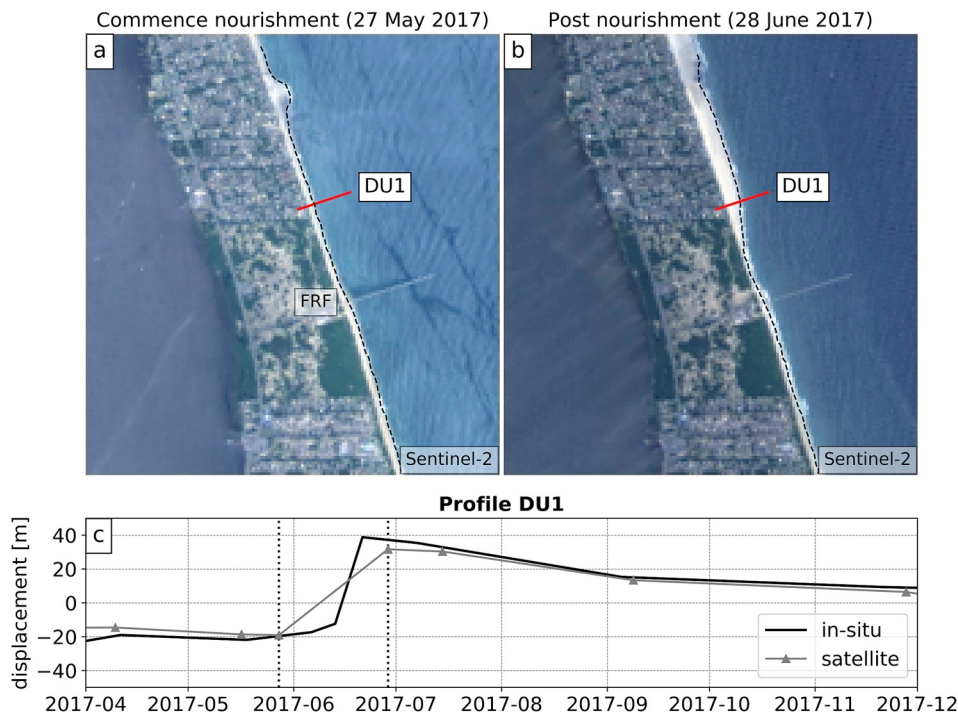


**Fig. 10.** a) Satellite image of Duck acquired at the commencement of the nourishment project (27 May 2017). b) Satellite image of Duck acquired upon completion of the nourishment (28 June 2017). c) Time-series of shoreline cross-shore displacement along transect DU1 obtained from in-situ surveys and satellite-derived shorelines.

took place over a short time period of one month, resulted in a shoreline accretion of 60 m that exceeds the satellite accuracy of 9.0 m (Fig. 6b) at this site. The sudden shoreline progradation was captured by the June and July 2017 satellite images. For the several months following the nourishment, satellite derived shorelines captured the 40 m of erosion due to cross-shore and longshore sediment transport processes occurring at the site.

## 5. Discussion

The detailed analyses presented here of satellite-derived shorelines obtained from five diverse study sites across three continents, indicate that this publicly available data set is suitable to capture ( $\text{SNR} > 1$ ) patterns and trends in shoreline variability at timescales of typically 6 months and longer (Fig. 7b). The exception to this was identified along sandy coastlines where the underlying intra-annual to annual shoreline variance is relatively minor, in which case longer-term decadal variations in shoreline behaviour may be realistically observed and quantified. Additionally, more rapid shoreline changes that exceed the typical magnitude of variability for a particular site - such as shoreline retreat caused by major coastal storms (Fig. 9) or sand nourishment works (Fig. 10) were also found to be well captured by satellite-derived shorelines. These results demonstrate that the combined image pre-processing and shoreline extraction methodology outlined in sections 2.2 and 2.3 (as summarised in Fig. 3) show good promise at providing a low-cost solution to obtain long-term shoreline data spanning the past 30 years at many sites worldwide.

### 5.1. Comparison with previous shoreline detection techniques

The sub-pixel resolution shoreline extraction algorithm presented here is shown to be capable of extracting time-series of shoreline displacement from publicly available satellite imagery with a horizontal accuracy of  $\sim 10$  m across sites spanning diverse coastal settings, including a meso-macro tidal regime. At Narrabeen, where the longest in-situ data set is available for direct comparison, a mean RMSE of 8.2 m was obtained across all five historical survey transects, indicating a significant improvement compared to recent work by Luijendijk et al.

(2018) that reported an RMSE of 13.7 m for the identical data sets. This 60% reduction in RMSE is achieved by some major differences in the two shoreline detection techniques, including the use of single rather than image composites, plus the application of pansharpening/downsampling and tidal correction. Notably, a third (and the only other) study by Liu et al. (2017) that has similarly used the long-term survey data set at Narrabeen to compare to satellite-derived shorelines, obtained a mean RMSE of 9.5 m. The slight improvement of the present work compared to the similar approach described in Liu et al. (2017) can be attributed to the introduction here of the refined four-class pixel classification, which assists to make the technique more robust across different sites and multiple imagery by focusing specifically on the sand/water interface.

### 5.2. Influence of pixel resolution on satellite-derived shoreline accuracy

Perhaps surprisingly, Fig. 5c reveals that the accuracy of shorelines obtained from Landsat 5 images (pixel size of 30 m) is comparable to the accuracy obtained from the significantly higher resolution Sentinel-2 images (pixel size of 10 m). This result indicates that the sub-pixel resolution technique is successful at enhancing the accuracy of the shorelines derived from the older Landsat 5 images, but more importantly, points to the fact that pixel size is not the main source of error when extracting instantaneous shorelines from satellite imagery. This finding is consistent with the results from several recent studies (Hagenaars et al., 2018; Liu et al., 2017; Pardo-Pascual et al., 2018), where similarly, no significant difference in accuracy was found when comparing shorelines derived from Landsat 5, Landsat 7, Landsat 8 and Sentinel-2 imagery.

In addition to pixel resolution, potential sources of shoreline error include: 1) horizontal inaccuracy in the georeferencing of individual satellite images; 2) uncertainty caused by the necessity to project an instantaneous shoreline to a reference elevation using a time-invariant ‘characteristic’ beach face slope; and 3) inherent error due to wave runup influencing the position of the captured instantaneous waterline. As demonstrated in Almonacid-Caballer et al. (2017), the georeferencing accuracy can be improved by combining a high-resolution ortho-image of the study area and the satellite images in the Fourier domain.

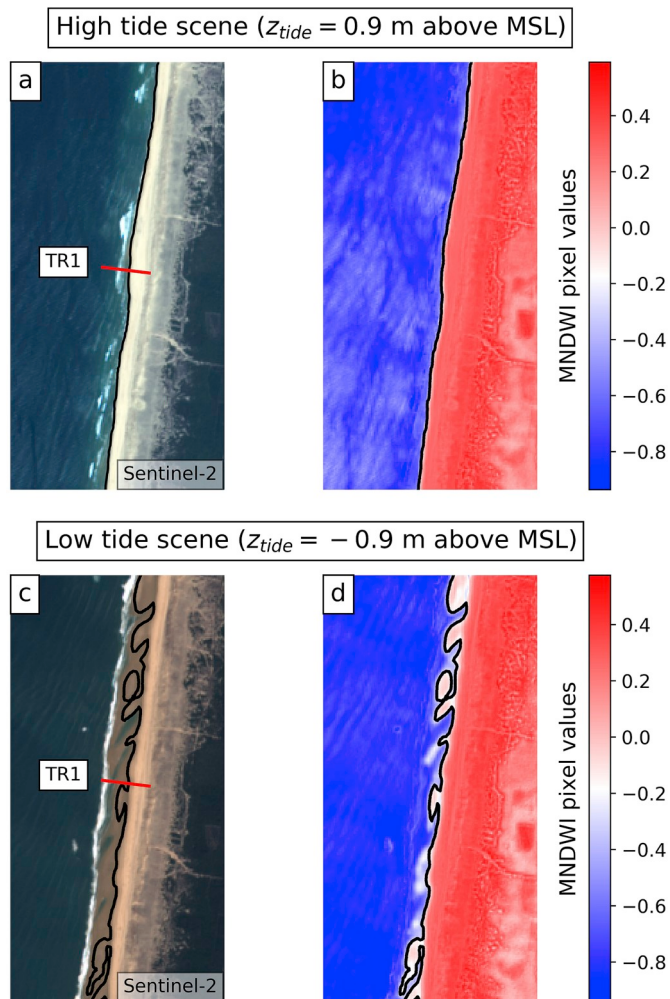


**Fig. 11.** a) RGB satellite image (Sentinel-2) acquired at high tide. b) Grayscale (i.e., single colour band) image of the Modified Normalized Difference Water Index (MNDWI) for the image acquired at high tide. c) RGB satellite image (Sentinel-2) acquired at low tide. d) Grayscale image of the MNDWI for the image acquired at low tide. (For interpretation of the references to colour in this figure legend, the reader is referred to the Web version of this article.)

The other two sources of error, however, are intrinsic to the definition of the ‘shoreline’ as the visibly discernible sand/water interface (Boak and Turner, 2005) and therefore depend on the instantaneous and localised water level (tide, setup, and runup) alongshore at the instant of image acquisition. The approach outlined here to incorporate a ‘characteristic’ beach face slope to implement tidal correction necessarily assumes stationarity in beach face morphology. But of course, the intertidal beach slope is a function of incident wave conditions and varies over time. For example, Madsen and Plant (2001) reported a standard deviation of ~25% of its mean value for the measured beach slope at Duck. To further evaluate this sensitivity to the assumption of a constant slope, the approximately fortnightly satellite-derived shorelines at Narrabeen were re-processed so that individual tidal correction of each image was performed using a time-varying slope, derived from the closest in-situ survey obtained between 0 and 10 days before/after each individual image acquisition. Interestingly, no significant improvement in the error statistics was found compared to using the single slope value, indicating the inherent challenge at dynamic sites, where daily and alongshore variability in beach face slope is anticipated.

Finally, wave runup is an aleatory motion of the waterline driven by the landward propagation of breaking waves and it cannot be corrected for directly on individual satellite images. Larger waves (wave height

and wave period) are responsible for increased wave setup and runup (Stockdon et al., 2006) and consequently may cause larger horizontal errors in the detected instantaneous shorelines. However, new technology in the form of miniaturised satellites (i.e., only ~100 kg) already offer the possibility to record high-resolution colour video from space (D’Angelo et al., 2014; Da Silva Curiel et al., 2018). The potential to obtain video streams from satellites will in the near future likely enable the application of time-averaged images to remove much of the influence of instantaneous wave runup on mapped shoreline positions, as has been common practice for the past two decades using terrestrial video-monitoring systems (e.g., Plant et al., 2007).

### 5.3. Shoreline detection at meso-macrotidal sites

To reduce the errors related to cloud cover and wave runup, Hagenars et al. (2018) aggregated multiple satellite images over time with an image composite technique (also employed by Luijendijk et al., 2018) in their global assessment of yearly shoreline change to assess long-term trends. However, a disadvantage of this approach is the resulting loss of temporal resolution, and it is clearly not appropriate to aggregate multiple images at sites where the instantaneous shoreline is primarily dependant on large tidal variations. For this reason, beaches along meso-macrotidal coastlines present particular challenges for satellite remote sensing (Almar et al., 2012). To illustrate, Fig. 11 depicts two example satellite images of Truc Vert (France) acquired at high tide ( $z_{tide} = 0.9$  m AMSL) and low tide ( $z_{tide} = -0.9$  m AMSL), shown here both as RGB and MNDWI images. While the detection algorithm is capable of extracting the shoreline accurately within the high tide scene (Fig. 11a and b), for the low tide scene (Fig. 11c and d), the presence of intertidal bars, shoals and troughs makes it extremely difficult to uniquely identify the position of the shoreline. Shallow pools of residual water fill depressions within the complex intertidal topography, surrounding the intertidal bars and creating small ‘sand islands’ (i.e., emergent intertidal sand bars). Under these circumstances, the instantaneous waterline meanders significantly and is not an especially useful indicator of the actual shoreline for the purposes of time-series variability and change analyses. To circumvent this particular challenge, at meso-macrotidal sites a practical solution is to extract satellite-derived shorelines from only those images that are captured at higher stages of the tide.

## 6. Conclusion

This paper has assessed the capability of satellite remote sensing to resolve differing temporal scales of shoreline variability that are of interest to coastal engineers, scientists and managers. Shorelines were extracted from 30+ years of publicly available imagery using a sub-pixel resolution technique, incorporating a new four-class classification procedure to better define the sand-water threshold. To demonstrate the generic application of this approach, time-series of shorelines were mapped at five long-term monitoring sites across three continents that between them exhibit a diverse range of beach characteristics including beach slope, tidal range and wave energy. The cross-shore accuracy of satellite-derived shorelines relative to field surveys was found to range from 7.3 m at a microtidal site with a steep beach face (Tairua, New Zealand) and up to 12.7 m at a meso-macrotidal site with a gentler sloping beach face (Truc Vert, France). At the Narrabeen site, the accuracy was found to be the smallest compared to previous studies using alternative satellite-derived shoreline extraction methods on the same dataset; highlighting the advantages of both sub-pixel resolution techniques combined with a new sand-water thresholding procedure for enhanced satellite-derived shoreline accuracy.

A detailed analysis of the magnitudes of shoreline variability at different timescales was undertaken by comparing shorelines obtained in the field over several decades to concurrent satellite-derived shorelines. The application of semivariogram analysis reveals that the

presently-available satellite imagery can be used to resolve (signal-to-noise ratio > 1) typical shoreline variability of around 6 months and longer. The exception to this is along coastlines where minimal sub-annual to annual shoreline variability occurs; at these sites decadal-scale variations are captured. This key finding demonstrates that satellite-derived shorelines can be used to examine intra- and inter-annual shoreline behaviour at a wide range of beaches around the world where a measurable shoreline variance is present. Clearly identified beach rotation signals at the Narrabeen and Moruya study sites demonstrate the potential for satellite-derived analyses to further investigate the characteristics and forcing of the beach rotation phenomenon, as well as other drivers of sandy shoreline seasonal to multi-year variability at many beaches worldwide. Rapid shoreline change events where these exceed the typical magnitudes of shoreline variability at a site can also be captured, illustrated here by the identification of extreme beach erosion resulting from a major storm, and the quantification of shoreline progradation due to localised sand nourishment works.

With satellite remote sensing capabilities continuously and rapidly improving each year, it is likely that finer spatial and temporal scales of shoreline variability beyond those identified in this study will be able to be resolved. This technological evolution will likely see an expansion of the way coastlines are monitored worldwide. As demonstrated in this study and elsewhere, a key aspect to rapidly advancing this transition is the need for making high-resolution satellite data both publicly available using open data protocols and accessible through cloud computing tools such as Google Earth Engine. The existing 30 + years of publicly available Landsat and Sentinel-2 data, combined with sophisticated shoreline extraction techniques, will be vital in underpinning these growing shoreline datasets into the future.

## Acknowledgments

The authors would like to thank B. Castelle (CNRS/Univ. Bordeaux) who kindly agreed to share the Truc Vert dataset (beach profiles and water levels), which is supported by the Service National d'Observation (SNO) Dynalit with surveys funded by various means throughout the years, including projects CHIPO (ANR-14-ASTR-0004-01) and SONO (ANR-17-CE01-0014) from the Agence Nationale de la Recherche (ANR), Observatoire Aquitain des Sciences de l'Univers (OASU) and Observatoire de la Côte Aquitaine (OCA). Thanks to Waikato Regional Council, NIWA, K. Bryan (Univ. of Waikato), G. Coco (Univ. of Auckland) and J. Montano (Univ. of Auckland) for making the Tairua data set available (daily shorelines and water levels). We acknowledge A.D. Short (Univ. of Sydney) for providing the Moruya shoreline data set. We also thank K. Brodie and the U.S. Army Engineer Research & Development Centre, Coast & Hydraulics Laboratory, Field Research Facility for making available the Duck in-situ data (beach profiles and water levels). Funding for the routine monitoring at Narrabeen is generously provided by Northern Beaches Council (formerly Warringah Council), UNSW Research Infrastructure Scheme, UNSW Faculty of Engineering Early Career Grant, the NSW Adaptation Research Hub – Coastal Processes Node (Office of Environment and Heritage), and the Australian Research Council (LP0455157, LP100200348, DP150101339, LP170100161). Manly Hydraulics Laboratory provided tide data on behalf of the NSW Office of Environment and Heritage for the two Australian study sites. The authors also appreciate the efforts of the United States Geological Survey and the European Space Agency in providing high-quality open-access data to the scientific community and Google Earth Engine for facilitating the access to the archive of publicly available satellite imagery.

## Appendix A. Supplementary data

Supplementary data to this article can be found online at <https://doi.org/10.1016/j.coastaleng.2019.04.004>.

## References

- Aagaard, T., Kroon, A., Andersen, S., Sørensen, R.M., Quartel, S., Vinther, N., 2005. Intertidal beach change during storm conditions; Egmond, The Netherlands. Mar. Geol. 218, 65–80. <https://doi.org/10.1016/j.margeo.2005.04.001>.
- Abrams, M., Hook, S., 2002. ASTER user handbook version 2. Jet Propuls 135. 2003. <https://doi.org/10.1017/CBO9781107415324.004>.
- Almar, R., Ranasinghe, R., Sénechal, N., Bonneton, P., Roelvink, D., Bryan, K.R., Marieu, V., Parisot, J.-P., 2012. Video-based detection of shorelines at complex meso-macro tidal beaches. J. Coast. Res. 284, 1040–1048. <https://doi.org/10.2112/JCOASTRES-D-10-00149.1>.
- Almonacid-Caballer, J., Pardo-Pascual, J.E., Ruiz, L.A., 2017. Evaluating fourier cross-correlation sub-pixel registration in Landsat images. Rem. Sens. 1051. <https://doi.org/10.3390/rs9101051>.
- Almonacid-Caballer, J., Sánchez-García, E., Pardo-Pascual, J.E., Balaguer-Beser, A.A., Palomar-Vázquez, J., 2016. Evaluation of annual mean shoreline position deduced from Landsat imagery as a mid-term coastal evolution indicator. Mar. Geol. 372, 79–88. <https://doi.org/10.1016/j.margeo.2015.12.015>.
- Barnard, P.L., Hoover, D., Hubbard, D.M., Snyder, A., Ludka, B.C., Allan, J., Kaminsky, G.M., Ruggiero, P., Gallien, T.W., Gabel, L., McCandless, D., Weiner, H.M., Cohn, N., Anderson, D.L., Serafin, K.A., 2017. Extreme oceanographic forcing and coastal response due to the 2015–2016 El Niño. Nat. Commun. 8. <https://doi.org/10.1038/ncomms14365>.
- Barnard, P.L., Short, A.D., Harley, M.D., Splinter, K.D., Vitousek, S., Turner, I.L., Allan, J., Banno, M., Bryan, K.R., Doria, A., Hansen, J.E., Kato, S., Kuriyama, Y., Randall-Goodwin, E., Ruggiero, P., Walker, I.J., Heathfield, D.K., 2015. Coastal vulnerability across the pacific dominated by El Niño/southern oscillation. Nat. Geosci. 8, 801–807. <https://doi.org/10.1038/geo2539>.
- Belward, A.S., Skøien, J.O., 2015. Who launched what, when and why: trends in global land-cover observation capacity from civilian earth observation satellites. ISPRS J. Photogrammetry Remote Sens. 103, 115–128. <https://doi.org/10.1016/j.isprsjprs.2014.03.009>.
- Blossier, B., Bryan, K.R., Daly, C.J., Winter, C., 2016. Nearshore sandbar rotation at single-barred embayed beaches. J. Geophys. Res. Ocean. 121, 2286–2313. <https://doi.org/10.1002/2016JC011882.Received>.
- Boak, E.H., Turner, I.L., 2005. Shoreline definition and detection: a review. J. Coast. Res. 214, 688–703. <https://doi.org/10.2112/03-0071.1>.
- Castelle, B., Guillot, B., Marieu, V., Chaumillon, E., Hanquiez, V., Bujan, S., Poppeschi, C., 2018. Spatial and temporal patterns of shoreline change of a 280-km high-energy disrupted sandy coast from 1950 to 2014: SW France. Estuar. Coast Shelf Sci. 200, 212–223. <https://doi.org/10.1016/j.ecss.2017.11.005>.
- Castelle, B., Marieu, V., Bujan, S., Ferreira, S., Parisot, J., Capo, S., Sénechal, N., Chouzenoux, T., 2014. Equilibrium shoreline modelling of a high-energy meso-macrotidal. Mar. Geol. 347, 85–94. <https://doi.org/10.1016/j.margeo.2013.11.003>.
- Chander, G., Markham, B.L., Helder, D.L., 2009. Summary of current radiometric calibration coefficients for Landsat MSS, TM, ETM+, and EO-1 ALI sensors. Remote Sens. Environ. 113, 893–903. <https://doi.org/10.1016/j.rse.2009.01.007>.
- Cipolletti, M.P., Delrieux, C.A., Perillo, G.M.E., Cintia Piccolo, M., 2012. Superresolution border segmentation and measurement in remote sensing images. Comput. Geosci. 40, 87–96. <https://doi.org/10.1016/j.cageo.2011.07.015>.
- D'Angelo, P., Kuschk, G., Reinartz, P., 2014. Evaluation of skybox video and still image products. Int. Arch. Photogramm. Remote Sens. Spat. Inf. Sci. - ISPRS Arch. 40, 95–99. <https://doi.org/10.5194/isprarchives-XL-1-95-2014>.
- Da Silva Curiel, A., Haslehurst, A., O'Brien, K., Navaratnam, N., Prasad, S., Saunders, C., Bird, R., Sills, L., Cawthron, A., Gomes, L., Sweeting, M., 2018. Watching the world go by. In: Proc. AIAA/USU Conf. Small Satell. SSC18-II-0, pp. 1–9. <https://doi.org/https://digitalcommons.usu.edu/smallsat/2018/TPS02-2018/1/>.
- Dolan, R., Hayden, P.B., May, P., May, S.K., 1980. The reliability of shoreline change measurements from aerial photographs. Shore Beach 48, 22–29.
- Douglas, B.C., Crowell, M., 2000. Long-term shoreline position prediction and error propagation. J. Coast. Res. J. Coast. Res. 16, 145–152.
- Elliot, J.R., Walters, R.J., Wright, T.J., 2016. The role of space-based observation in understanding and responding to active tectonics and earthquakes. Nat. Commun. 7, 1–16. <https://doi.org/10.1038/ncomms13844>.
- Emery, K.O., 1961. A simple method of measuring beach profile. Limnol. Oceanogr. 6, 90–93.
- ESA, 2015. SENTINEL-2 User Handbook. <https://doi.org/GMES-S1OP-EOPG-TN-13-0001>.
- Gorelick, N., Hancher, M., Dixon, M., Ilyushchenko, S., Thau, D., Moore, R., 2017. Google earth engine: planetary-scale geospatial analysis for everyone. Remote Sens. Environ. 202, 18–27. <https://doi.org/10.1016/j.rse.2017.06.031>.
- Hagenaars, G., de Vries, S., Luijendijk, A.P., de Boer, W.P., Reniers, A.J.H.M., 2018. On the accuracy of automated shoreline detection derived from satellite imagery: a case study of the sand motor mega-scale nourishment. Coast. Eng. 133, 113–125. <https://doi.org/10.1016/j.coastaleng.2017.12.011>.
- Harley, M.D., Andriolo, U., Armaroli, C., Ciavola, P., 2014. Shoreline rotation and response to nourishment of a gravel embayed beach using a low-cost video monitoring technique: san Michele-Sassi Neri, Central Italy. J. Coast. Conserv. 18, 551–565. <https://doi.org/10.1007/s11852-013-0292-x>.
- Harley, M.D., Turner, I.L., Kinsela, M.A., Middleton, J.H., Mumford, P.J., Splinter, K.D., Phillips, M.S., Simmons, J.A., Hanslow, D.J., Short, A.D., 2017. Extreme coastal erosion enhanced by anomalous extratropical storm wave direction. Sci. Rep. 7, 6033. <https://doi.org/10.1038/s41598-017-05792-1>.
- Harley, M.D., Turner, I.L., Short, A.D., 2015. New insights into embayed beach rotation: the importance of wave exposure and cross-shore processes. J. Geophys. Res. F Earth

- Surf. 120, 1470–1484. <https://doi.org/10.1002/2014JF003390>.
- Harley, M.D., Turner, I.L., Short, A.D., Ranasinghe, R., 2011. Assessment and integration of conventional, RTK-GPS and image-derived beach survey methods for daily to decadal coastal monitoring. *Coast. Eng.* 58, 194–205. <https://doi.org/10.1016/j.coastaleng.2010.09.006>.
- Holland, K.T., Holman, R.A., Lippmann, T.C., Stanley, J., Plant, N., 1997. Practical use of video imagery in nearshore oceanographic field studies. *IEEE J. Ocean. Eng.* 22, 81–91. <https://doi.org/10.1109/48.557542>.
- Holman, R.A., Stanley, J., 2007. The history and technical capabilities of Argus. *Coast. Eng.* 54, 477–491. <https://doi.org/10.1016/j.coastaleng.2007.01.003>.
- Kanellopoulos, I., Wilkinson, G.G., 1997. Strategies and best practice for neural network image classification. *Int. J. Remote Sens.* 18, 711–725. <https://doi.org/10.1080/01431697218719>.
- Kuleli, T., Guneroglu, A., Karsli, F., Dihkan, M., 2011. Automatic detection of shoreline change on coastal Ramsar wetlands of Turkey. *Ocean Eng.* 38, 1141–1149. <https://doi.org/10.1016/j.oceaneng.2011.05.006>.
- Kuriyama, Y., 2002. Medium-term bar behavior and associated sediment transport at Hasaki, Japan. *J. Geophys. Res.* 107, 3132. <https://doi.org/10.1029/2001JC000899>.
- Lacey, E.M., Peck, J.A., Island, R., Lacey, E.M., Peck, J.A., 1998. Long-term beach profile variations along the south shore of Rhode Island. *U.S.A. J. Coast. Res.* 14, 1255–1264.
- Larson, M., Kraus, N.C., 1994. Temporal and spatial scales of beach profile change, Duck, North Carolina. *Mar. Geol.* 117, 75–94. [https://doi.org/10.1016/0025-3227\(94\)90007-8](https://doi.org/10.1016/0025-3227(94)90007-8).
- Liu, Q., Trinder, J., Turner, I.L., 2017. Automatic super-resolution shoreline change monitoring using Landsat archival data: a case study at Narrabeen-Collaroy Beach, Australia. *J. Appl. Remote Sens.* 11, 016036. <https://doi.org/10.1117/1.JRS.11.016036>.
- Luijendijk, A., Hagenaars, G., Ranasinghe, R., Baart, F., Donchyts, G., Aarninkhof, S., 2018. The state of the world's beaches. *Sci. Rep.* 1–11. <https://doi.org/10.1038/s41598-018-24630-6>.
- Madsen, A.J., Plant, N.G., 2001. Intertidal beach slope predictions compared to field data. *Mar. Geol.* 173, 121–139. [https://doi.org/10.1016/S0025-3227\(00\)00168-7](https://doi.org/10.1016/S0025-3227(00)00168-7).
- Masselink, G., Castelle, B., Scott, T., Dodet, G., Suanez, S., Jackson, D., Floc, F., 2016. Extreme wave activity during 2013/2014 winter and morphological impacts along the Atlantic coast of Europe. *Geophys. Res. Lett.* 2135–2143. <https://doi.org/10.1002/2015GL067492> (Received).
- Masselink, G., Pattiaratchi, C.B., 2001. Seasonal changes in beach morphology along the sheltered coastline of Perth, Western Australia. *Mar. Geol.* 172, 243–263. [https://doi.org/10.1016/S0025-3227\(00\)00128-6](https://doi.org/10.1016/S0025-3227(00)00128-6).
- Mentaschi, L., Vousdoukas, M.I., Pekel, J.-F., Voukouvalas, E., Feyen, L., 2018. Global long-term observations of coastal erosion and accretion. *Sci. Rep.* 8, 12876. <https://doi.org/10.1038/s41598-018-30904-w>.
- National Research Council, 1990. Managing Coastal Erosion. The National Academies Press, Washington, DC. <https://doi.org/10.17226/1446>.
- Objeda, E., Guillén, J., 2008. Shoreline dynamics and beach rotation of artificial embayed beaches. *Mar. Geol.* 253, 51–62. <https://doi.org/10.1016/j.margeo.2008.03.010>.
- Otsu, N., 1979. A threshold selection method from gray-level histograms. *IEEE Trans. Syst. Man Cybern.* 20, 62–66. [https://doi.org/0018-9472/79/0100-0062\\$00.75](https://doi.org/0018-9472/79/0100-0062$00.75).
- Pardo-Pascual, J.E., Sánchez-García, E., Almonacid-Caballer, J., Palomar-Vázquez, J.M., de los Santos, E.P., Fernández-Sarría, A., Balaguer-Beser, Á., 2018. Assessing the accuracy of automatically extracted shorelines on microtidal beaches from landsat 7, landsat 8 and sentinel-2 imagery. *Rem. Sens.* 10. <https://doi.org/10.3390/rs10020326>.
- Pianca, C., Holman, R.A., Siegle, E., 2015. Shoreline variability from days to decades: results of long-term video imaging. *J. Geophys. Res. Ocean.* 1–17. <https://doi.org/10.1002/2014JC010320> (Received).
- Plant, N.G., Aarninkhof, S.G.J., Turner, I.L., Kingston, K.S., 2007. The performance of shoreline detection models applied to video imagery. *J. Coast. Res.* 233, 658–670. [https://doi.org/10.2112/1551-5036\(2007\)23\[658:TPOSDM\]2.0.CO;2](https://doi.org/10.2112/1551-5036(2007)23[658:TPOSDM]2.0.CO;2).
- Ranasinghe, R., McLoughlin, R., Short, A., Symonds, G., 2004. The Southern Oscillation Index, wave climate, and beach rotation. *Mar. Geol.* 204, 273–287. [https://doi.org/10.1016/S0025-3227\(04\)00002-7](https://doi.org/10.1016/S0025-3227(04)00002-7).
- Różyński, G., 2005. Long-term shoreline response of a nontidal, barred coast. *Coast. Eng.* 52, 79–91. <https://doi.org/10.1016/j.coastaleng.2004.09.007>.
- Sénéchal, N., Gouriou, T., Castelle, B., Parisot, J.P., Capo, S., Bujan, S., Howa, H., 2009. Morphodynamic response of a meso- to macro-tidal intermediate beach based on a long-term data set. *Geomorphology* 107, 263–274. <https://doi.org/10.1016/j.geomorph.2008.12.016>.
- Short, A.D., Bracs, M.A., Turner, I.L., 2014. Beach oscillation and rotation: local and regional response at three beaches in southeast Australia. *J. Coast. Res.* 712–717. <https://doi.org/10.2112/SI65-xxx.1>.
- Short, A.D., Trembanis, A.C., 2004. Decadal scale patterns in beach oscillation and rotation narrabeen beach, Australia—time series, PCA and wavelet analysis. *J. Coast. Res.* 20, 523–532. [https://doi.org/10.2112/1551-5036\(2004\)020\[0523:DSPIBO\]2.0.CO;2](https://doi.org/10.2112/1551-5036(2004)020[0523:DSPIBO]2.0.CO;2).
- Stockdon, H.F., Asbury Jr., H., S, List, J.H., Holman, R.A., 2002. Estimation of shoreline position and change using airborne topographic lidar data. *J. Coast. Res.* 18, 502–513. <https://doi.org/10.2307/4299097>.
- Stockdon, H.F., Holman, R.A., Howd, P.A., Sallenger, A.H., 2006. Empirical parameterization of setup, swash, and runup. *Coast. Eng.* 53, 573–588. <https://doi.org/10.1016/j.coastaleng.2005.12.005>.
- Tu, T.-M., Su, S., hu, -C., Shyu, H., Huang, P.S., 2001. A new look at IHS-like image fusion methods. *Inf. Fusion* 2, 177–186. [https://doi.org/10.1016/S1566-2535\(01\)00036-7](https://doi.org/10.1016/S1566-2535(01)00036-7).
- Turner, I.L., Harley, M.D., Drummond, C.D., 2016a. UAVs for coastal surveying. *Coast. Eng.* 114, 19–24. <https://doi.org/10.1016/j.coastaleng.2016.03.011>.
- Turner, I.L., Harley, M.D., Short, A.D., Simmons, J.A., Bracs, M.A., Phillips, M.S., Splinter, K.D., 2016b. A multi-decade dataset of monthly beach profile surveys and inshore wave forcing at Narrabeen, Australia. *Sci. data* 3, 160024. <https://doi.org/10.1038/sdata.2016.24>.
- USGS, 2017. *Landsat Collection 1 Level 1 Product Definition*.
- Van de Lageweg, W.I., Bryan, K.R., Coco, G., Ruessink, B.G., 2013. Observations of shoreline-sandbar coupling on an embayed beach. *Mar. Geol.* 344, 101–114. <https://doi.org/10.1016/j.margeo.2013.07.018>.
- Vos, K., Splinter, K.D., Harley, M.D., Simmons, J.A., Turner, I.L., 2019. *CoastSat: a Python toolkit to extract shorelines from publicly available satellite imagery*. *Environ. Model. Softw.* in review.
- Wijnberg, K.M., Terwindt, J.H.J., 1995. Extracting decadal morphological behaviour from high-resolution, long-term bathymetric surveys along the Holland coast using eigenfunction analysis. *Mar. Geol.* 126, 301–330. [https://doi.org/10.1016/0025-3227\(95\)00084-C](https://doi.org/10.1016/0025-3227(95)00084-C).
- Wright, L.D., Short, A.D., 1984. Morphodynamic variability of surf zones and beaches: a synthesis. *Mar. Geol.* 56, 93–118. [https://doi.org/10.1016/0025-3227\(84\)90008-2](https://doi.org/10.1016/0025-3227(84)90008-2).
- Xu, H., 2006. Modification of normalised difference water index (NDWI) to enhance open water features in remotely sensed imagery. *Int. J. Remote Sens.* 27, 3025–3033. <https://doi.org/10.1080/0143160600589179>.
- Xu, N., 2018. Detecting coastline change with all available landsat data over 1986–2015: a case study for the state of Texas , USA. *Atmosphere* 9, 107. <https://doi.org/10.3390/atmos9030107>.